Reformulating Compressed Sensing to be used with Semi-Resolved Point Spread Function and Light Curves for Space Object Imaging: LEO

Daigo Kabayashi and Carolin Frueh
School of Aeronautics and Astronautics, Purdue University
dkobayas@purdue.edu,cfrueh@purdue.edu

Abstract

Optical observations are a cost-efficient way of collecting information about human-made space objects. Ideally, a fully resolved image of any satellite and space-debris object could be created from observations without other guiding information. The challenges are two-fold. Firstly, the distance between the observer and the objects is generally large relative to the size of the objects; secondly, in ground-based observations, atmospheric turbulence affects the measurements. *Compressed sensing* (CS) is a technique well-established in image compression. Under the condition of sparsity, a resolved image can be recovered from a compressed version, containing only a subset of the information of the original high-resolution image. In this paper, the classical CS framework is modified to be used for space-object characterization. This paper focuses on objects in Low-Earth orbit, where semi-resolved imaging is available. However, the images are heavily degraded by atmospheric turbulence. The paper shows a high-fidelity simulation of the atmospheric effect on the light propagation of a Low-Earth Orbit (LEO) space object. A new CS-based reconstruction algorithm has been developed to recover a fully resolved image based on the simulated light curve and the atmospheric point spread function (PSF). The effect of uncertainty in the PSF is explicitly shown, and the robustness of the method is highlighted. The method applies to large LEO objects that are stabilized during the time of observation.

1. INTRODUCTION

Today, there are more than 100 million space objects around the near-Earth space environment [1] greater than 1 mm. Larger objects can be observed in a cost-efficient manner using ground-based optical sensors. Electro-optical measurements can not only be used to determine orbits and infer trajectory information but also to characterize aspects of the bodies beyond their center of mass. Light curve measurements are a temporal history of the light intensity reflected off a space object [2, 3, 4]. The shape, attitude, and surface parameters are superimposed in a light curve. Light curve inversion for human-made space objects is well-investigated [5, 6, 7, 8, 9, 10, 11, 12, 13, 14, 15, 16, 17, 18, 19, 20, 21, 22, 23, 24, 25, 26, 27, 28, 29, 30, 31, 32]. However, the problem is plagued with non-uniqueness inherent to the problem, and the high dimensionality of the solution: three-dimensional shape information with n number of facets with potentially unique surface parameters and a six-parametric rotational state. The states can be reduced by requiring further assumptions on attitude, albedo shape, or a simplified attitude motion [5, 6, 7, 8, 9, 10, 11, 12, 13, 14, 15, 16, 17, 18, 19, 20, 21, 22, 23, 24, 25, 26, 27, 28, 29, 30, 31]. Alternatively, the states may be reduced by not reconstructing a three-dimensional state with material properties but a two-dimensional image with a frozen attitude state, which is the option explored in this paper leveraging methods known from compressed sensing.

Compressed sensing is a signal processing framework that uses sparsity to compress and recover a signal most efficiently [33], [34]. A high-dimensional signal is mapped to a lower-dimensional signal via a so-called sensing matrix. The sensing matrix needs to satisfy the Restricted Isometry Property and is typically designed to have random entries. If the signal is sparse in a particular basis, the signal can be recovered by finding a solution with the smallest L_1 norm that results in the compressed signal. Compressed sensing shows its true worth when it allows recovering an original signal or image from a limited number of measurements that is significantly lower than the Nyquist/Shannon sampling theorem limit.

In previous work by the authors [32], the recovery of a resolved image of an unknown space object has been achieved based on its light curve using multiplicative noise, which is regarded as a sensing matrix.

This paper develops a more rigorous model of light curve degradation by generating the atmospheric point spread function (PSF) in an anisoplanatic imaging simulation. An LEO object is assumed to be observed from the ground under the influence of atmospheric turbulence. First, a spherical wave is propagated from every point of an object through the free space up to the top of the atmosphere. The output wave is subsequently propagated through a set of phase screens that model the turbulence up to the center of the pupil of the PSF sensor. The propagated wave is then used to compute the PSF. The PSFs from each point of the object are then used to compute a theoretical, so-called pseudo, degraded image and corresponding light curve as observed from the aperture-limited ground-based telescope. Finally, the sensing matrix that maps the original object to the light curve is computed, and the recovered image is derived. In the paper, several scenarios of PSF degradation are shown: from using the exact PSF to the heavily degraded one.

2. PRELIMINARIES

2.1 Optical Transfer Function

The optical transfer function (OTF) is the Fourier transform of a PSF. The OTF of the imaging system that consists of an optical path through atmosphere and an optical lens system is given by

$$H(\rho) = H_{\text{atm}}(\rho) H_{\text{dif}}(\rho) \tag{1}$$

where $H_{\text{atm}}(\rho)$ is the atmospheric OTF and $H_{\text{dif}}(\rho)$ is the diffraction-limited OTF of the optical lens system. Note that these OTFs are both assumed to be circularly symmetric, and hence they are the functions of the radial spatial frequency, $\rho = \sqrt{f_x^2 + f_y^2}$ where f_x and f_y are the spatial frequency in x and y direction respectively.

The atmospheric OTF [35] is given by

$$H_{\text{atm}}(\rho) = \exp\left\{ -3.44 \left(\frac{\lambda f_\ell \rho}{r_0} \right)^{5/3} \left[1 - \alpha \left(\frac{\lambda f_\ell \rho}{D} \right)^{1/3} \right] \right\} \tag{2}$$

where λ is the wavelength, f_ℓ is the camera's focal length, r_0 is the coherence diameter [36], and D is the aperture diameter. The parameter α works as a switch of three different exposure conditions [37]:

$$\alpha = \begin{cases} 0 & \text{for long-exposure imagery} \\ 1 & \text{for short-exposure imagery without scintillation} \\ \frac{1}{2} & \text{for short-exposure imagery with scintillation} \end{cases} \tag{3}$$

The short exposures and long exposures are different in the way the atmospheric tilt is corrected. In both cases, the image center wanders randomly in the image plane. In the long-exposure imagery, the exposure is assumed to be long enough to average out the random tilts. In the short-exposure imagery, on the other hand, the exposure is so short that the image is affected by only one realization of tilt.

The diffraction-limited OTF for a circular aperture is given by

$$H_{\text{dif}}(\rho) = \begin{cases} \frac{2}{\pi} \left[\cos^{-1}\left(\frac{\rho}{\rho_c} \right) - \frac{\rho}{\rho_c} \sqrt{1 - \left(\frac{\rho}{\rho_c} \right)^2} \right], & \rho \le \rho_c \\ 0, & \text{otherwise} \end{cases} \tag{4}$$

where $\rho_c = 1/(\lambda f_n)$ is the optical cut-off frequency, and the f_n is the f-number: $f_n = f_\ell / D$.

2.2 Bandwidth and Nyquist Spacing

The anisoplanatic imaging simulation uses a two-dimensional discrete Fourier transform. The Nyquist grid spacing for the discrete models of object and PSFs needs to be carefully considered to avoid aliasing errors.

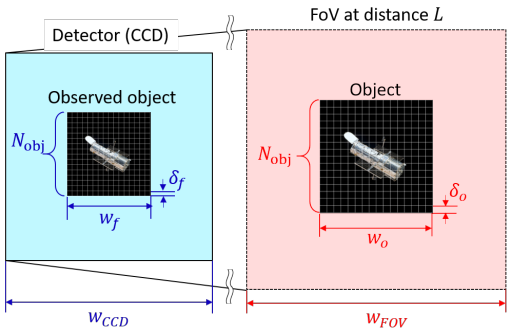

Figure 1: Schematic of the relationship between the image on a detector and the actual object size.

First, the Nyquist grid spacing of PSF is considered. As discussed in the Sec.2.1, the Fourier spectrum of the PSF, or the OTF has a cut-off frequency of ρ_c. In other words, it is strictly band-limited with the bandwidth of $2\rho_c$. Therefore, the Nyquist spacing of the PSF is given by:

$$\delta_f = \frac{1}{2\rho_c} = \frac{\lambda f_\ell}{2D} \tag{5}$$

Second, the Nyquist spacing of the object model is considered. In the strict sense, the Nyquist spacing completely depends on the object model that is used. Alternatively, this study considers the pixel spacing of the object model such that the image of the object observed on a detector has a Nyquist spacing, δ_f. Figure 1 shows the one-to-one relationship of the image on a detector and the actual object. The field of view (FoV) of a telescope is given by

$$FoV = \tan^{-1}\left(\frac{w_{CCD}}{f_\ell}\right) \approx \frac{w_{CCD}}{f_\ell} \tag{6}$$

where w_{CCD} is the side width of the detector. Thus, the width of the FoV is

$$w_{FoV} \approx FoV \cdot L = \frac{L\, w_{CCD}}{f_\ell} \tag{7}$$

where L is the distance between the detector and the object. On the other hand, the side length of the object image on CCD is

$$w_f = N_{obj}\delta_f = \frac{N_{obj}\lambda f_\ell}{2D} \tag{8}$$

Since the ratio between the width of the FoV and the actual object size should be preserved on the detector, it follows that

$$\frac{w_o}{w_{FoV}} = \frac{w_f}{w_{CCD}} \tag{9}$$

Therefore, the side length of the actual object is obtained by equating Eqs.6 - 9:

$$w_o = w_f \frac{w_{FoV}}{w_{CCD}} = \frac{N_{obj}\lambda f_\ell}{2D}\,\frac{L\, w_{CCD}/f_\ell}{w_{CCD}} = \frac{\lambda L}{2D} N_{obj} \tag{10}$$

Thus, the Nyquist spacing of the object model is computed by

$$\delta_o = \frac{w_o}{N_{obj}} = \frac{\lambda L}{2D} \tag{11}$$

Hereinafter, this grid spacing is used when modeling the object discretely.

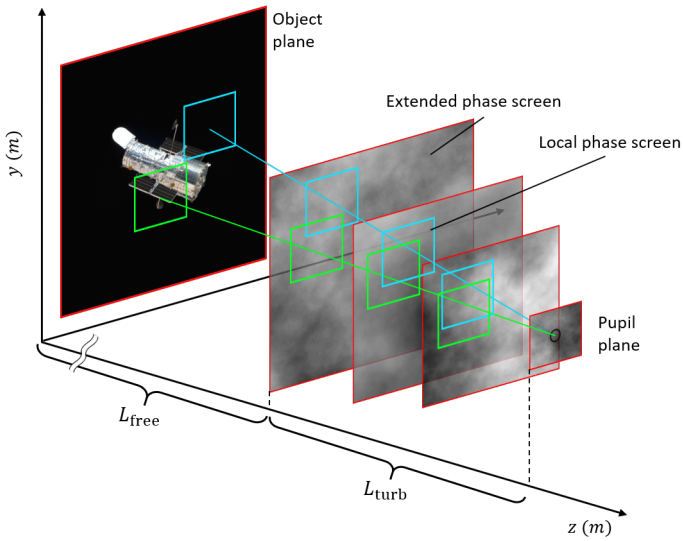

Figure 2: Geometry of the optical wave propagation of a LEO object.

3. LIGHT PROPAGATION MODELING

3.1 Overview

The numerical wave propagation through free space and turbulence is simulated for an LEO object. First, a spherical wave is emitted from every point of the object plane and propagated through free space over distance L_{free}, where there exists almost no atmosphere. Subsequently, the optical wave is propagated through the atmospheric turbulence from the upper atmosphere to the ground. The random phase fluctuation due to the turbulence is modeled as a set of extended phase screens that are equally spaced over distance L_{turb}. The extended phase screens are modeled discretely by an array of size $\mathcal{N}_{\text{ext}} \times \mathcal{N}_{\text{ext}}$. They are cropped to generate local phase screens of size $\mathcal{N} \times \mathcal{N}$ $(< \mathcal{N}_{\text{ext}})$, within a predefined distance of the optical path from each point of the object. Figure 2 shows two sets of local phase screens as blue and green squares. Finally, the propagated wave is used to compute a point spread function (PSF) corresponding to each point of the object.

Ideally, the PSFs are computed for all the pixels of the object plane. However, to save computational time, the PSFs are instead computed at sample points spaced by small pixel values (e.g, four pixels) in the object plane. The PSF values at the non-sample points are computed by bilinear interpolation, which still preserves the spatial correlation of the atmospheric turbulence.

After computing the spatially-varying PSFs, the degraded image of the object is computed by the spatially-weighted average of the true object. The degraded image is the theoretical image of a PSF sensor, which may or may not be identical to the ground-based telescope that is used for the imaging. This paper assumes that the ground-based sensor has aperture and hence resolution, leading to an entirely unresolved image formed into a noise-affected, degraded light curve. The degraded light curve is computed as the pixel summation of the degraded image. Therefore, the light curve measurement is a linear mapping of the true object because of the linearity of the spatially-weighted average computation. This linear light curve model is interpreted as a linearly-compressed image in compressed sensing with a sensing matrix whose row is the spatial variations of PSFs.

The anisoplanatic imaging simulation used in this paper is an extension to free space and long-distance propagation of the work by Hardie et al. [38], where the anisoplanatic imaging through the turbulence for short distances of 7 km is introduced.

In the following subsections, more details about these procedures are described. In Section 3.2, the theories and procedures to generate the extended phase screens are explained. In Section 3.3, the numerical wave propagation method of each spherical wave from the object is described. In Section 3.4, the computation of PSF, the degraded image, and the degraded light curve is detailed. In Section 3.5, the anisoplanatic imaging model is compared with the

compressed sensing, and the sensing matrix is obtained. In Section 4, the recovery of the resolved image from the light curve is shown.

3.2 Phase Screen Realizations

3.2.1 Coherence Diameter of Each Phase Screen

The atmospheric coherence diameter introduced by Fried [36] is the diameter, for which the turbulence starts to seriously distort the optical field. For a spherical wave, the diameter is computed as

$$r_0 = \left[0.423k^2 \int_0^L C_n^2(z) \left(\frac{z}{L}\right)^{5/3} \, \mathrm{d}z\right]^{-3/5} \tag{12}$$

where $k = 2\pi/\lambda$ is the wavenumber, λ is the wavelength, and L is the propagation distance. C_n^2 is the structure parameter, which is a measure of the local turbulence strength [35]. The coherence diameter is typically of the order of several centimeters.

The isoplanatic angle is an angular separation with which two point sources will have approximately the same PSF. The isoplanatic angle is related to the integral of the $C_n^2(z)$ parameter:

$$\theta_0 = \left[2.91k^2L^{5/3} \int_0^L C_n^2(z) \left(1 - \frac{z}{L}\right)^{5/3} \, \mathrm{d}z\right]^{-3/5} \tag{13}$$

The log-amplitude variance related to fluctuations in the optical wave amplitude, is given by:

$$\sigma_\chi^2 = 0.563k^{7/6}L^{5/6} \int_0^L C_n^2(z) \left(\frac{z}{L}\right)^{5/6} \left(1 - \frac{z}{L}\right)^{5/6} \, \mathrm{d}z \tag{14}$$

Each layer of the atmosphere is discretely modeled as a phase screen with a local coherent diameter. Its coherence diameter is assumed to be expressed as:

$$r_{0_i} = \left[0.423k^2 C_{n_i}^2 \Delta z_i\right]^{-3/5} \tag{15}$$

Solving Eq.15 in terms of $C_{n_i}^2$ and substituting into the discrete versions of Eqs.12 - 14, it follows that

$$\hat{r}_0 = \left[\sum_{i=1}^{N} 0.423k^2 C_{n_i}^2 \left(\frac{z_i}{L}\right)^{5/3} \Delta z_i\right]^{-3/5} = \left[\sum_{i=1}^{N} (r_{0_i})^{-5/3} \left(\frac{z_i}{L}\right)^{5/3}\right]^{-3/5} \tag{16}$$

$$\hat{\theta}_0 = \left[2.91k^2L^{5/3} \sum_{i=1}^{N} \left(C_{n_i}^2\right) \left(1 - \frac{z_i}{L}\right)^{5/3} \Delta z_i\right]^{-3/5} = \left[\sum_{i=1}^{N} L^{5/3} \left(1 - \frac{z_i}{L}\right)^{5/3} 6.8794 \, (r_{0_i})^{-5/3}\right]^{-3/5} \tag{17}$$

$$\hat{\sigma}_\chi^2 = 0.563k^{7/6}L^{5/6} \sum_{i=1}^{N} C_{n_i}^2 \left(\frac{z_i}{L}\right)^{5/6} \left(1 - \frac{z_i}{L}\right)^{5/6} \Delta z_i = 1.331 \left(\frac{L}{k}\right)^{5/6} \sum_{i=1}^{N} (r_{0_i})^{-5/3} \left(\frac{z_i}{L}\right)^{5/6} \left(1 - \frac{z_i}{L}\right)^{5/6} \tag{18}$$

Note that the second terms of the equations are the discrete versions of the parameter values, and the third terms are the results after the $C_{n_i}^2$ parameter is eliminated. Combining Eqs.16-18, a linear matrix equation is obtained as below:

$$\begin{bmatrix} (\hat{r}_0)^{-5/3} \\ \frac{\hat{\sigma}_\chi^2}{1.331k^{-5/6}L^{5/6}} \\ \frac{\left(\hat{\theta}_0\right)^{-5/3}}{6.8794L^{5/3}} \end{bmatrix} = \begin{bmatrix} \left(\frac{z_1}{L}\right)^{5/3} & \left(\frac{z_2}{L}\right)^{5/3} & \cdots & \left(\frac{z_N}{L}\right)^{5/3} \\ \left(\frac{z_1}{L}\right)^{5/6} \left(1 - \frac{z_1}{L}\right)^{5/6} & \left(\frac{z_2}{L}\right)^{5/6} \left(1 - \frac{z_2}{L}\right)^{5/6} & \cdots & \left(\frac{z_N}{L}\right)^{5/6} \left(1 - \frac{z_N}{L}\right)^{5/6} \\ \left(1 - \frac{z_1}{L}\right)^{5/3} & \left(1 - \frac{z_2}{L}\right)^{5/3} & \cdots & \left(1 - \frac{z_N}{L}\right)^{5/3} \end{bmatrix} \begin{bmatrix} r_{0_1}^{-5/3} \\ \vdots \\ r_{0_N}^{-5/3} \end{bmatrix} \tag{19}$$

Given the positions of phase screens and the values of $\hat{r}_0$, $\hat{\sigma}_\chi^2$, and $\hat{\theta}_0$ parameters, the left-hand side and the first term of the right-hand side in Eq.19 are known. Therefore, the local coherence diameter value $r_{0_i}^{-5/3}$ can be obtained by

solving a constrained least squares optimization problem:

$$\begin{aligned} \min_{\mathbf{s}} \quad & \|\hat{\mathbf{b}} - \mathbf{A}\mathbf{s}\|_2^2 \\ \text{s.t.} \quad & 1.331 k^{-5/6} L^{5/6} \left(\frac{z_i}{L}\right)^{5/6} \left(1 - \frac{z_i}{L}\right)^{5/6} \leq 0.2\hat{\sigma}_\chi^2 \\ & 0 \leq r_{0_i}, \quad \forall i = 1, \ldots, N \end{aligned}$$

where $\hat{\mathbf{b}}$ is the left-hand side of Eq.19. The matrix $\mathbf{A}$ and the vector $\mathbf{s}$ are the first and second terms of the right-hand side of Eq.19.

3.2.2 Monte-Carlo Phase Screens

The extended phase screens can be computed by Monte Carlo method after computing the coherence diameter of each phase screen. The following expression holds when assuming the turbulence-induced optical phase $\phi(x,y)$ can be written as a Fourier series:

$$\phi(x,y) = \sum_{n=-\infty}^{\infty} \sum_{m=-\infty}^{\infty} c_{n,m} \exp\left[i2\pi(f_{x_n} x + f_{y_m} y)\right], \tag{20}$$

where f_{x_n} and f_{y_m} are the spatial frequencies in the x and y directionsm respectively, and $c_{n,m}$ are the Fourier series coefficients. The extended phase screens are designed such that the coefficients $c_{n,m}$ have a Gaussian distribution with a zero mean and a variance given by [37]:

$$\langle |c_{n,m}|^2 \rangle = S_\phi^{mvK}(f_{x_n}, f_{y_m}) \Delta f_{x_n} \Delta f_{y_m}, \tag{21}$$

where $\langle \cdot \rangle$ denotes the ensemble average, and Δf_{x_n} and Δf_{y_m} are the frequency spacings in the x and the y directions, respectively. The term S_ϕ^{mvK} is a modified von Karman phase power spectral density (PSD). The PSD for the i-th phase screen is given by [37]:

$$S_{\phi_i}^{mvK}(\rho) = \frac{0.023 e^{-\rho^2/\rho_m^2}}{r_{0_i}^{5/3} (\rho^2 + \rho_0^2)^{11/6}}, \tag{22}$$

where $\rho = \sqrt{f_x^2 + f_y^2}$ is the radial spatial frequency, r_{0_i} is the coherence diameter of the phase screen, and $\rho_m = 5.92/(2\pi\ell_0)$ and $\rho_0 = 1/L_0$ are the coefficients with respect to the outer scale L_0 and the inner scale ℓ_0, respectively. Turbulent eddies are randomly-distributed pockets of air due to the non-uniform velocity distribution. The outer and inner scales are the average sizes of the largest and smallest turbulent eddies.

Therefore, the procedures for generating the phase screen is the following: First, the parameter r_{0_i} for each phase screen is obtained by the method described in Sec.3.2.1. Based on these values, the modified von Karman phase PSD

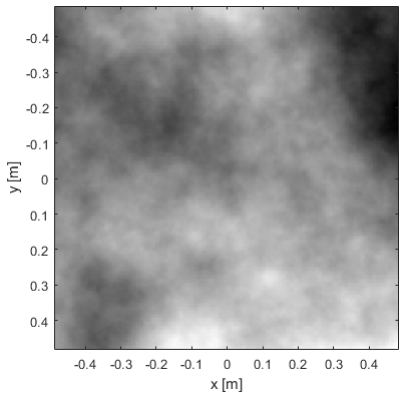

Figure 3: Example of the extended phase screen.

is computed by Eq.22. This value is used to generate a white Gaussian variable with variance given by Eq.21. Finally, based on Eq.20, the fast Fourier transform (FFT) is used to generate the phase screens. However, this FT method does not produce an accurate statistics of the phase screens.

The subharmonic method described by Lane et al. [39] is implemented for the computation of a higher fidelity phase screen. In this method, a high-frequency and low-frequency component are computed separately. The high-frequency phase screen is computed by Eq.20. A low-frequency phase screen is generated as a sum of N_p different screens, given by:

$$\phi_{LF}(x,y) = \sum_{p=1}^{N_p} \sum_{n=-1}^{1} \sum_{m=-1}^{1} c_{n,m} \exp\left[i2\pi(f_{x_n}x + f_{y_m}y)\right] \tag{23}$$

The random draws of the Fourier coefficients are generated at N_p times with different grid spacings of $\Delta f_p = 1/(3^p W)$, where W is the width of the sampling grid. This sampling allows generating a screen with varieties of frequency components. The low-frequency phase screen $\phi_{LF}(x,y)$ is then added to the high-frequency phase screen. Figure 3 shows one example of the extended phase screen.

3.3 Numerical Wave Propagation

The split-step propagation method for generating a PSF that corresponds to one sample point of the object is illustrated in Figure 4. It involves a spherical wave and a set of N local phase screens that are cropped from the extended phase screens based on the geometry as shown in Figure 2.

First, the wave propagation through the free space over distance L_{free} is considered. The point source is modeled by a Dirac delta function:

$$u_{\text{pt}}(x,y) = \delta(x,y) \tag{24}$$

The wave after free-space propagation is computed by the Fresnel diffraction integral [37]:

$$u_0(x,y) = \frac{e^{jkL_{\text{free}}}}{j\lambda L_{\text{free}}} \int_{-\infty}^{\infty}\int_{-\infty}^{\infty} u_{\text{pt}}(x_{\text{pt}},y_{\text{pt}}) e^{j\frac{k}{2L_{\text{free}}}\left[(x_{\text{pt}}-x)^2+(y_{\text{pt}}-y)^2\right]} dx_{\text{pt}}dy_{\text{pt}} = \frac{e^{jkL_{\text{free}}}}{j\lambda L_{\text{free}}} e^{j\frac{k}{2L_{\text{free}}}\left(x^2+y^2\right)} \tag{25}$$

Second, the propagation through turbulence of a distance L_{turb} is considered. The wave field is propagated through the phase screens and free space sequentially by

$$u_i(x,y;t) = \left[u_{i-1}(x,y;t) * h_{\Delta z_i}(x,y)\right] e^{j\phi_i(x,y;t)}, \tag{26}$$

for $i = 1,2,\ldots,N$ where the operation $A * B$ represents a 2D convolution of A and B. Note that $\phi_i(x,y;t)$ is the turbulence-induced random phase fluctuation that is modeled by the i-th phase screen, which is a function of time t depending on a wind function. The term $h_{\Delta z_i}$ is the impulse response of free-space propagation for Fresnel diffraction

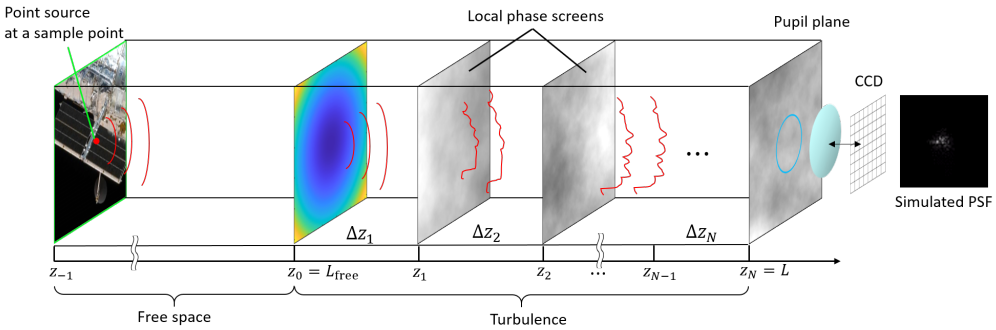

Figure 4: Illustration of the split-step propagation of a spherical wave from a sample point of an object.

between the $(i-1)$-th and the i-th phase screens:

$$h_{\Delta z_i}(x,y) = \frac{e^{jk\Delta z_i}}{j\lambda\Delta z_i} e^{j\frac{k}{2\Delta z_i}(x^2+y^2)} \tag{27}$$

Eq.26 is implemented by angular spectrum method described by Schmidt [37], which uses the fast Fourier transform (FFT) to compute the 2D convolution. To accelerate the FFT, the number of discrete sample points of phase screens, $\mathscr{N}$ is chosen to be a power of two. The sampling grid spacing of phase screens is determined by the critical sampling size proposed by Volez [40]:

$$\delta = \left(\frac{\lambda L_{\text{turb}}}{\mathscr{N}}\right)^{1/2} \tag{28}$$

This grid spacing gives the best use of bandwidth for Fresnel propagation simulation while avoiding an aliasing problem.

3.4 Incoherent Point Spread Function

After the propagation simulation, the complex amplitude at the pupil plane, $u_N(x,y)$ is obtained. The generalized pupil function is computed by:

$$p(x,y;t) = a(x,y)\; u_N(x,y;t)\; e^{-\frac{j\pi(x^2+y^2)}{\lambda L}} \tag{29}$$

where $a(x,y)$ is the circular aperture mask denoted by

$$a(x,y) = \begin{cases} 1 & \sqrt{x^2+y^2} \le D/2 \\ 1/2 & \sqrt{x^2+y^2} = D/2 \\ 0 & \sqrt{x^2+y^2} > D/2 \end{cases} \tag{30}$$

Note that D is the aperture diameter of the PSF sensor, and $L = L_{\text{free}} + L_{\text{turb}}$ is the total propagation distance. The last exponential term in Eq.29 is the collimation effect by a lens. The incoherent PSF, $h(x,y;t)$ is obtained by computing the Fourier transform of the generalized pupil function, and then computing the squared magnitude of the result:

$$P(f_x,f_y;t) = \mathscr{F}\{p(x,y;t)\} \tag{31}$$

$$h(x,y;t) = \left[\left|P(f_x,f_y;t)\right|^2\right]\Big|_{f_x=\frac{x}{\lambda f_\ell}, f_y=\frac{y}{\lambda f_\ell}} \tag{32}$$

where f_ℓ is the focal length of the PSF sensor. The resultant incoherent PSF is then normalized to have a sum of 1.

The incoherent PSFs are computed for the point sources at all the sample points spaced by four pixels. The incoherent PSFs for the other point sources of the object plane are computed, as mentioned before, by bilinear interpolation method as illustrated in Figure 5. Given the incoherent sample PSFs at points $Q_{11} = (x_1,y_1)$, $Q_{21} = (x_2,y_1)$, $Q_{12} = (x_1,y_2)$, and $Q_{22} = (x_2,y_2)$, the incoherent PSF at a point $P = (x,y)$ in the square $Q_{11}Q_{21}Q_{22}Q_{12}$ is computed by:

$$\tilde{h}(x,y;t) = w_{11}h(x_1,y_1;t) + w_{21}h(x_2,y_1;t) + w_{12}h(x_1,y_2;t) + w_{22}h(x_2,y_2;t) \tag{33}$$

where w_{ij}'s are the weight of each sample PSF:

$$w_{11} = \frac{(x_2-x)(y_2-y)}{(x_2-x_1)(y_2-y_1)},\; w_{21} = \frac{(x-x_1)(y_2-y)}{(x_2-x_1)(y_2-y_1)},\; w_{12} = \frac{(x_2-x)(y-y_1)}{(x_2-x_1)(y_2-y_1)},\; w_{22} = \frac{(x-x_1)(y-y_1)}{(x_2-x_1)(y_2-y_1)}$$

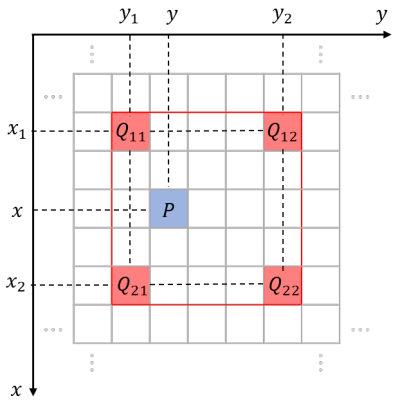

Figure 5: Schematic diagram of the bilinear interpolation used for PSF computation.

3.5 Degraded Image, Light Curve, and Sensing Matrix

In the isoplanatic imaging, a PSF is space-invariant and hence a degraded image can be computed by a 2D convolution between a true object image and the PSF. In the anisoplanatic imaging, however, the PSF is not space-invariant anymore. Therefore, the degraded image is computed by a sum of the object image spatially weighted by PSFs. The pixel value of the degraded image at point (μ,ν) at time t is given by:

$$z(\mu,\nu;t) = \sum_k \sum_l o(\mu-k,\nu-\ell) h_{\mu,\nu}(k,\ell;t) \tag{34}$$

where $o(\mu,\nu)$ is the true object image, and $h_{\mu,\nu}(k,\ell;t)$ is the space-variant PSF associated with the point source at the point (μ,ν) of the true object image at time t.

The grid spacing of the object model and the PSF needs to be adjusted to the same values before computing Eq.34. As mentioned in Sec.2.2, the object is imaged on the PSF detector as a discrete model with a grid spacing of δ_f. On the other hand, the grid spacing of the PSF obtained by Eq.32 is

$$\delta_{PSF} = \frac{\lambda f_\ell}{\delta_{\mathscr{N}}} \tag{35}$$

which is not equal to δ_f. Therefore, the result of Eq.32 is resampled to the grid spacing of δ_f before implementing Eq.34. Finally, the degraded image result is resampled to the grid spacing of the detector to get the final image. In the resampling computation, a pixel binning instead of interpolation is used to preserve the sum of the pixel values.

The light curve intensity, or the brightness of a non-resolved telescope image at time t_j is a summation of pixel values of the degraded image:

$$y_j = \sum_\mu \sum_\nu z(\mu,\nu;t_j) \tag{36}$$

which is in the units of W/m^2. The light curve is simply a time sequence of such intensity measurements at m time steps:

$$\mathbf{y} = \begin{bmatrix} y_1 & y_2 & \dots & y_m \end{bmatrix}^T \tag{37}$$

Finally, the light curve model in Eq.36 and the image model in Eq.34 are adapted to compressed sensing. First, the spatially-weighted summation in Eq.34 is interpreted as a matrix operation, as shown in Figure 6. Suppose we want to compute the pixel value at a point (μ,ν) of the image. Then, the centroid of the corresponding PSF is shifted to the point (μ,ν). The object model and the shifted PSF is multiplied pixel-wise, and the pixel summation of the result is computed and assigned to $z(\mu,\nu)$. These operations are given by:

$$z(\mu,\nu) = \sum_{\text{pixels}} o \odot h_{\mu,\nu,\text{shifted}} \tag{38}$$

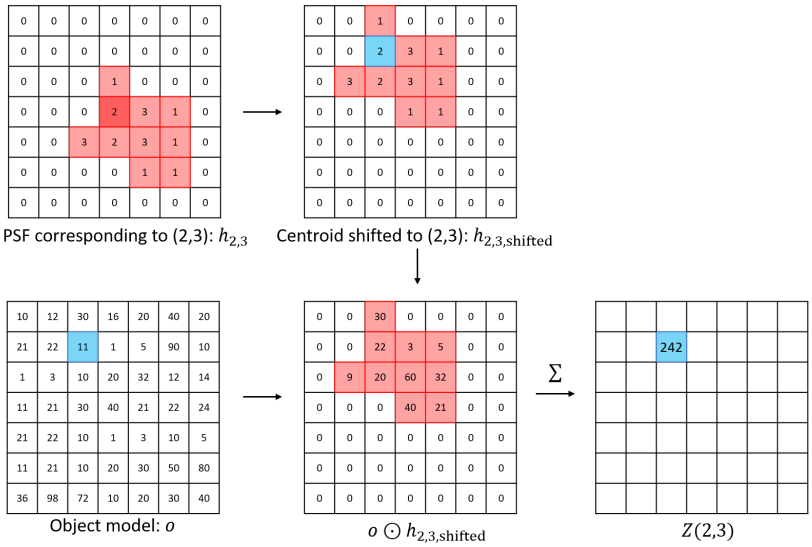

Figure 6: Example of the computation of a pixel of the degraded image.

where $\odot$ is a pixel-wise product operator, o is the object model, and $h_{\mu,\nu,\text{shifted}}$ is the shifted PSF. Both o and $h_{\mu,\nu,\text{shifted}}$ are modeled as matrices but they can be reshaped into vectors. Let $\mathbf{x}$ and $\mathbf{h}_\iota$ be the vector form of o and $h_{\mu,\nu,\text{shifted}}$ respectively, it follows that

$$z(\mu,\nu) = \mathbf{h}_\iota^T \mathbf{x} \tag{39}$$

where ι is the linear index of the point (μ,ν). Therefore, a vector form of the degraded image model, $\mathbf{z}$ can be expressed linearly in terms of $\mathbf{x}$:

$$\mathbf{z} = \begin{bmatrix} \mathbf{h}_1^T \mathbf{x} \\ \mathbf{h}_2^T \mathbf{x} \\ \vdots \end{bmatrix} = \begin{bmatrix} \mathbf{h}_1^T \\ \mathbf{h}_2^T \\ \vdots \end{bmatrix} \mathbf{x} \tag{40}$$

As in Eq.36, the light curve intensity is the summation of the entries of $\mathbf{z}$, which can be expressed as:

$$y_j = \mathbf{1}^T \mathbf{z} = \mathbf{1}^T \begin{bmatrix} \mathbf{h}_1^T \\ \mathbf{h}_2^T \\ \vdots \end{bmatrix} \mathbf{x}, \tag{41}$$

where $\mathbf{1}^T = [1\ 1\ \ldots\ 1]$ is an all-1's vector. Comparing Eq.41 with Eq.43, a row of the sensing matrix is found to be the superposition of all the shifted PSFs given by:

$$\boldsymbol{\phi}_j^T = \mathbf{1}^T \begin{bmatrix} \mathbf{h}_1^T \\ \mathbf{h}_2^T \\ \vdots \end{bmatrix} \tag{42}$$

Therefore, a row of the sensing matrix represents the spatial variations of PSFs, named a PSF map. The sensing matrix is an interal element in the compressed sensing methodology [32].

4. IMAGE RECOVERY BY USING THE DANTZIG SELECTOR

The reconstruction algorithm developed here uses the compressed sensing scheme in order to recover a truthful image. As the input, the measured light curve and the PSF map from the PSF sensor are used.

First, the mathematical formulation of the problem is explained. The light curve measurement at m time steps, denoted as $\mathbf{y} \in \mathbb{R}^m$, can be understood as a linear transformation of the true object image ($\mathbf{x} \in \mathbb{R}^N$, $m \ll N$) by a sensing matrix $\Phi \in \mathbb{R}^{m \times N}$:

$$\mathbf{y} = \Phi \mathbf{x} \tag{43}$$

Each row of the sensing matrix ($\phi_j^T \in \mathbb{R}^N$) is the PSF map at each time step, t_j for $j = 1, \ldots, m$. Since the number of measurements, m, is usually much smaller than N, this system is underdetermined.

Candes, Donoho, and Romberg [41] [33] [34] showed that it is possible to solve this underdetermined system by finding a vector with the minimum ℓ_1 norm that explains the measurement:

$$\hat{\gamma} = \arg\min_{\gamma} \|\gamma\|_1 \quad \text{s.t. } \|\mathbf{y} - \Phi\Psi\gamma\|_2 \leq \varepsilon \tag{44}$$

$$\mathbf{x} \approx \Psi\gamma \quad \text{s.t. } \|\gamma\|_1 \ll N, \tag{45}$$

where ε is an error bound, and $\Psi \in \mathbb{R}^{N \times N}$ is a so-called dictionary, which is a basis to sparsify the vector $\mathbf{x}$. The solution $\hat{\gamma}$ is a sufficiently sparse vector such that $\mathbf{y} = \Phi\Psi\gamma + \mathbf{e}$ for some small error term $\|\mathbf{e}\|_2 \leq \varepsilon$. This error term is called the sparse representation error (SRE).

The traditional approach just outlined has two major challenges. The first problem is the computational cost. The size of the image vector tends to be $N \sim 10^5$. It is computationally expensive to solve Eq.44 even for a small number of m. There are some fast solvers available for this problem, but they tend to sacrifice the reconstruction accuracy.

The second problem is the ill-designed sensing matrix Φ in this study. In the traditional approach, the equivalent dictionary $\Phi\Psi$ is chosen so that it follows the Restricted Isometry Property (RIP), which guarantees the nearly perfect reconstruction of the image $\mathbf{x}$. In contrast, in the LEO imaging problem, a PSF map is used as the sensing matrix, which is purely the result of atmospheric turbulence and is found not to satisfy the RIP condition, leading to inaccurate reconstruction using Eq.44.

The following two solutions are explored in this paper: The first problem can be eased by narrowing down the region where the object of interest resides in the image plane. The object location can be estimated from the combination of the Airy disk imaging of the light curve in combination with a background correction and removal.

The second problem can be alleviated by solving a more robust alternative that is referred to as the Dantzig selector [42]:

$$\hat{\gamma}_I = \arg\min_{\gamma_I} \|\gamma_I\|_1 \quad \text{s.t. } \|\mathbf{D}_I^*(\mathbf{y} - \mathbf{D}_I\gamma_I)\|_2 \leq \varepsilon \tag{46}$$

The Dantzig selector approach requires that the SRE ($= \mathbf{y} - \mathbf{D}_I\gamma_I$) is not significantly correlated with any of the columns of $\mathbf{D}_I$. If the SRE follows a Gaussian distribution with variance σ^2 then the solution of the Dantzig Selector is nearly optimal with a loss within a logarithmic factor of the ideal mean squared error [42] of oracle solution:

$$E\|\hat{\gamma}_I - \gamma_0\|_2^2 \leq C(\log N) \cdot \sum_i \min(\gamma_0(i)^2, \sigma^2), \tag{47}$$

where γ_0 denotes the oracle solution.

In this paper, the image of the LEO object of interst is recovered by solving the problem described by Eq.46. The problem is recast as second-order cone programs (SOCPs) and solved by the implementations in Chapter 11 of [43]. The intensiveness of computation is eased by implicitly computing any large matrix operation by conjugate gradient method.

The resultant image is evaluated by an image quality metric called structural similarity (SSIM) index [44]. The SSIM matches the human perceived visual quality and is hence superior compared to other traditional image quality metrics such as the mean squared error (MSE) and the peak signal-to-noise ratio (PSNR). The SSIM represents the image quality in the range $[0, 1]$, where 0 denotes the worst and 1 denotes the best quality, respectively.

5. EXPERIMENTAL RESULTS

5.1 Anisoplanatic Imaging Illustration

Table 1: Simulation Parameters

Parameter	Value
Aperture diameter PSF sensor	$D = 0.61$ m
Focal length PSF sensor	$f_\ell = 6.25$ m
Wavelength	$\lambda = 525$ nm
Nyquist pixel spacing of phase screens	$\delta = 5.0630$ mm
Nyquist pixel spacing of PSFs	$\delta_f = 2.6895$ μm
Nyquist pixel spacing of object plane	$\delta_o = 0.1290$ m
Pixel spacing of detector (CCD)	$\delta_{\text{CCD}} = 5.5$ μm
Propagation distance through free space	$L_{\text{free}} = 250$ km
Propagation distance through turbulence	$L_{\text{turb}} = 50$ km
Propagation step in turbulence	$\Delta z = 5$ km
Number of phase screens	$N = 11$
Extended phase screen samples	$\mathscr{N}_{\text{ext}} = 3072$ pixels
Local phase screen samples	$\mathscr{N} = 1024$ pixels
Refractive index structure parameter	$C_n^2 = 1.0 \times 10^{-16}$ m$^{-2/3}$
Inner scale	$\ell_0 = 0.01$ m
Outer scale	$L_0 = 300$ m
Object model samples	257×257 pixels
Object plane side length	33.18 m
Pixel skip	4 pixels (65×65 PSF arrays)

The experimental simulations are implemented based on the simulation parameter values in Table 1. The true object that is chosen in the simulations is the Hubble Space Telescope (HST), [45].

First, a set of eleven extended phase screens is computed as described in Sec.3.2. The values of the coherence diameter and isoplanatic angle of the whole optical path are $r_0 = 0.0584$ m and $\theta_0 = 0.3675$ μrad, respectively. Based on these values, the parameter values of individual phase screens are computed by the constrained least squares optimization. The result of the coherence diameter of each extended phase screen is shown in Figure 8. Note that the last extended phase screen is constrained to have $r_{0_N} = \infty$ to avoid the excessive tilt correlation following the Hardie's approach [38].

Subsequently, the numerical wave propagation through free space and turbulence is implemented by procedures described in Sec.3.3. The spherical waves are propagated from sample points spaced by four pixels on the object plane of size 257×257 pixels. In other words, 65×65 spherical waves are propagated in total. To model an imaging of an object in LEO, the total propagation is set to be $L = 300$ km. Since the atmospheric turbulence has a significant effect in a region up to the altitude of 50km, the propagation distances through free space and turbulence are set to be $L_{\text{free}} = 250$ km and $L_{\text{turb}} = 50$ km respectively.

Figure 7: True object image [45].

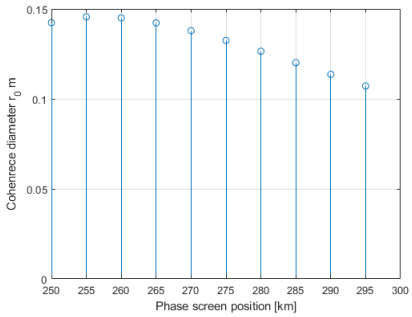

Figure 8: Atmospheric coherence diameter values for individual phase screens

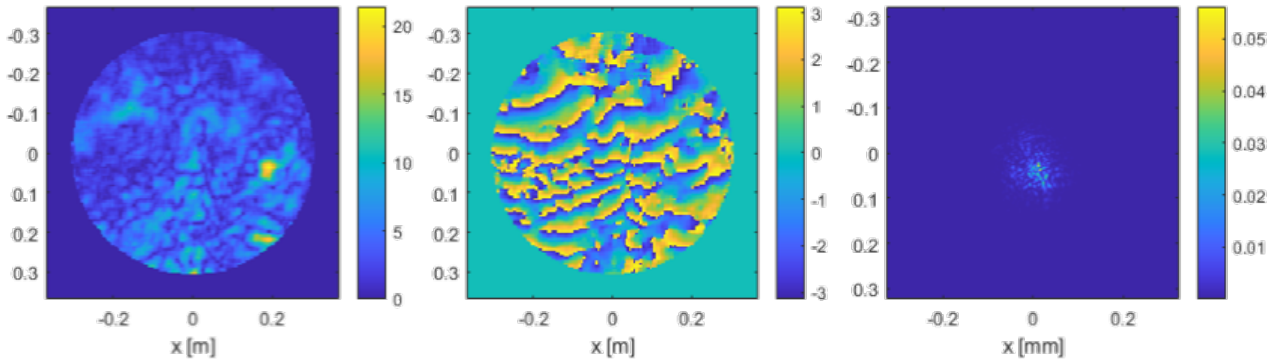

(a) (b) (c)

Figure 9: Example of the propagated wave and PSF: (a) Irradiance of the propagated wave, (b) Phase of the propagated wave, (c) Point spread function (PSF).

Figure 9 shows one example of the result of the propagated wave. The irradiance and phase of the propagated wave are well-sampled on the sampling grid. The smallest local phase screen sample size to avoid aliasing problem is found to be 1024 pixels. This large phase screen size slows down the computation of angular spectrum method, which needs to be repeated 65^2 times in one simulation. To speed up the computation, all the FFT computations are implemented on a GPU. As a result, the computation time for obtaining the whole image is shortened to 30 minutes.

The simulations are implemented for four different object sizes for illustration purposes: 15m, 10m, 6m, and 3m. Figure 10 shows the results of the degraded images as they would arrive by the PSF sensor.

For comparison, the simulation results of the numerical wave propagation only through free space are shown in the top row of Figure 10(a)-(d) and with atmosphere in the bottom row. Note that the total propagation distance is kept to be $L = 300$ km for a fair comparison. As can be seen, the turbulence significantly smears and warps the image while the free space propagation barely alters the details of the object appearance. Another noticable thing is that the shape of the object is still recognizable in (e) and (f) but it becomes barely recognizable in (g) and (h), where it is basically in the un-resolved regime already.

In the simulation at each time frame, the extended phase screens are shifted by several pixels to realize the temporal correlation of the optical turbulence effect for temporally-changing phase screens for 80 frames. The size of the screen shift is determined by assuming the wind speed is 1 m/s. The object size is fixed to 13.2m for this illustration. Figure 11 shows the results of the images and the corresponding PSF map at four time frames. As can be seen, the warping and brightness of the object change over time due to the random fluctuation of the PSFs. This results in the fluctuation of the intensity observed by the sensor. Figure 13 (a) shows the normalized light curve obtained by this simulation.

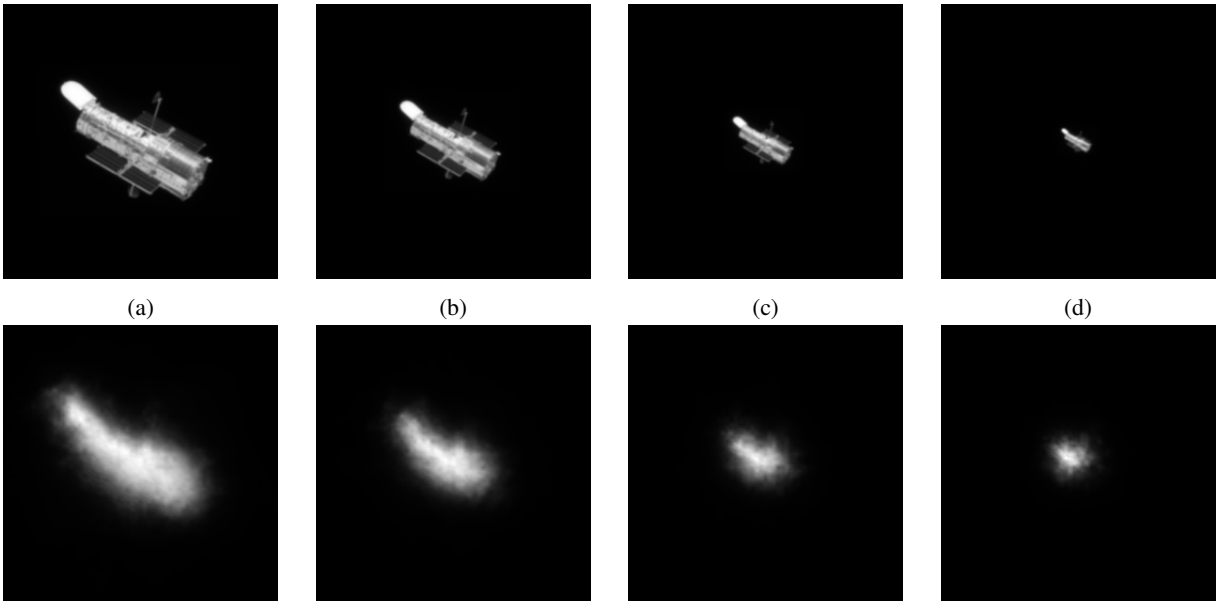

Figure 10: Comparison of degraded images with and without atmosphere. Top row: without atmosphere, bottom row: with atmosphere. Columns vary by object size: (a)&(e): 15m, (b)&(f): 10m, (c)&(g): 6m, (d)&(h): 3m.

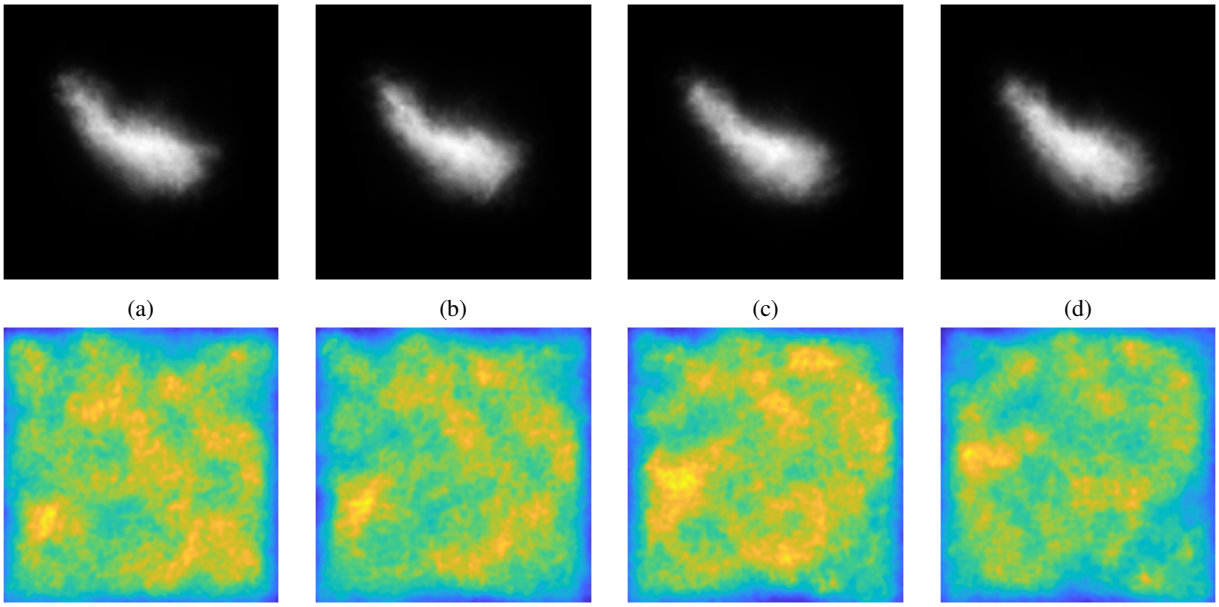

Figure 11: Time history of the degraded image and PSF map for object size of 13.2m with wind speed 1m/s blowing from bottom to left in the images, and a frame rate of 40 frames/second: (a) Image at frame 1, (b) Image at frame 10, (c) Image at frame 20, (d) Image at frame 30, (e) PSF map at frame 1, (f) PSF map at frame 10, (g) PSF map at frame 20, (h) PSF map at frame 30.

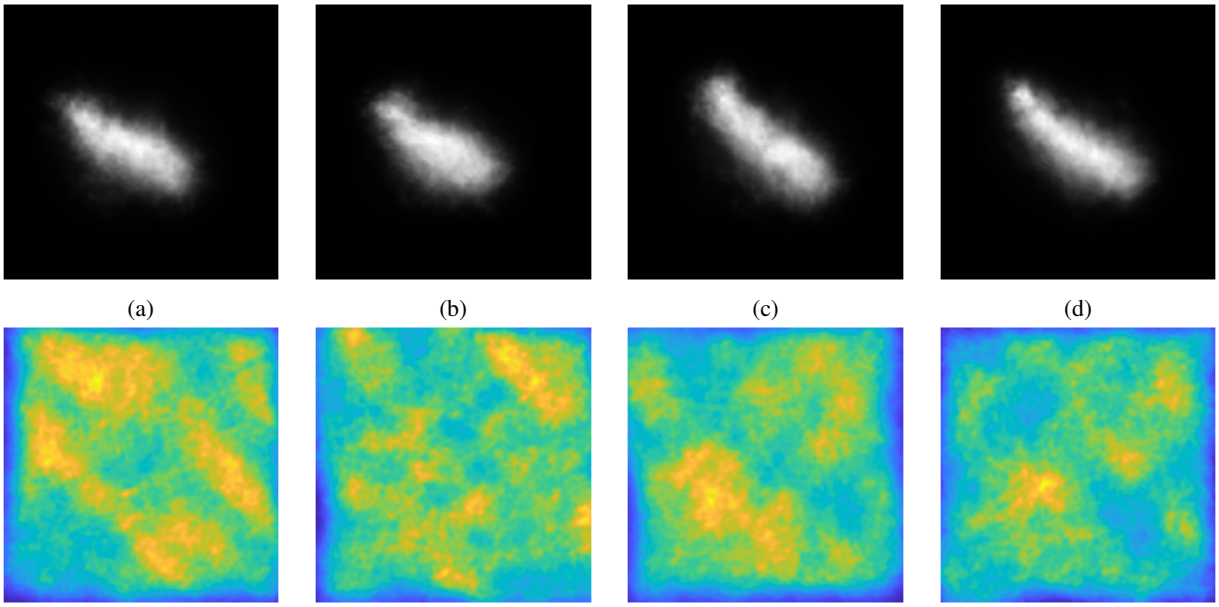

Figure 12: Time history of the degraded image and PSF map for object size of 13.2m with high wind speeds from bottom to left in the images, and a frame rate of 40 frames/second: (a) Image at frame 1, (b) Image at frame 10, (c) Image at frame 20, (d) Image at frame 30, (e) PSF map at frame 1, (f) PSF map at frame 10, (g) PSF map at frame 20, (h) PSF map at frame 30.

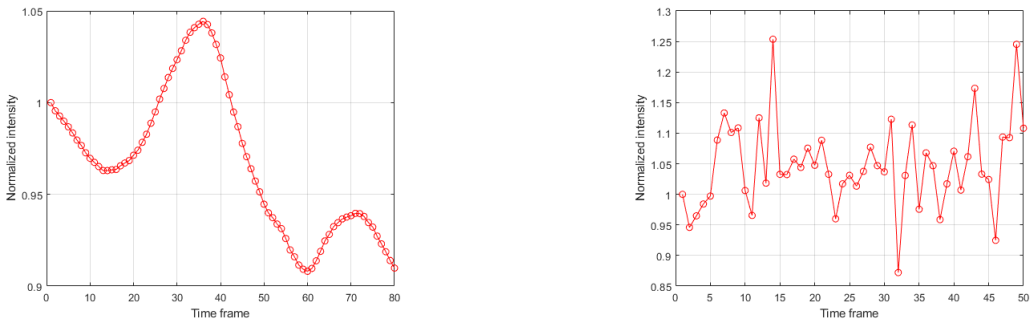

(a) (b)

Figure 13: Normalized light curve obtained by the anisoplanatic imaging simulation: (a) simulation results for 80 frames with wind speed 1m/s, (b) simulation results for 50 frames with temporally-uncorrelated phase screens, which corresponds to a faster wind speed.

The light intensity value is normalized by the intensity value at the first time frame for enhanced readability of the plot. Since the wind speed is very slow, the light curve fluctuates almost continuously. More realistically, the wind speed is the order of 10 m/s so the light should pass through a new set of turbulence layers that is independent from previous sets of layers. The Figure 12 shows the images and corresponding PSF map corresponding to high wind speeds. While on the PSF level the differences are deceivingly small, the corresponding light curve shown in Figure 13 (b) shows significant differences. Now, the phase screens are uncorrelated. As a result, the fluctuation of the intensity becomes more significant and discontinuous compared to Figure 13(a).

5.2 The Full Simulation and Recovery: Image Recovery by Dantzig Selector

For the following simulations, it is assumed that the imaging of the space object takes place such that the stabalized object's scene does not significantly change. This requires bright objects observed in rapid fashion, e.g., using CMOS sensing techniques. Only under those conditions a single image representing the observations can be found.

5.2.1 Perfect PSF Map

The experimental simulation is conducted to reconstruct the true LEO image in Figure 7 at an altitude of 300 km based on its light curve and the PSF maps. The object size is assumed to be most realistic 13.2 meters. High wind speeds are assumed to be most realistic, the PSF that has been used is the one shown in Fig.12, leading to the light curve shown in Fig.13(b).

The image size of the PSF map is 257×257. The simulation parameter values used are the same as listed in Table 1, where the ground-based optical sensor generating the light curve is assumed to have the same or a smaller aperture than the PSF sensor, as only the light curve information itself is extracted after simple background correction.

First, the degraded images of the LEO object and PSF maps are simulated for 2000 frames. The PSF maps are reshaped into vectors and concatenated to form a sensing matrix of size 2000×257^2. In this simulation, the light curve is, of course, degraded because of the passage through the atmosphere. However, in this first simulation it is assumed that the PSF map is perfectly known.

In each frame, a set of phase screens are generated such that the phase screens are identical and independent from that of the other frames to account for fast wind speeds. The non-resolved light curve is computed. The region of interest is applied to limit the number of pixels in the recovery.

The image is reconstructed by solving the Dantzig Selector problem. The tolerance for correlation is set to be 3e-3, the tolerance for primal-dual algorithm to be 5e-3, and the tolerance for conjugate gradients to be 1e-8. The reconstructed results are denoised by BM3D algorithm [46] to improve the image quality.

Figure 14 shows (a) the ideal image, (b) recovered image, and (c) denoised image. The images are color-coded for better visibility. Even in the recovered image, the main body and the aperture door are clearly recognizable. The SSIM index of the recovered image is 0.772. The denoised image has even better quality with SSIM index of 0.932, and it clearly shows the solar panels that are darker than the main body.

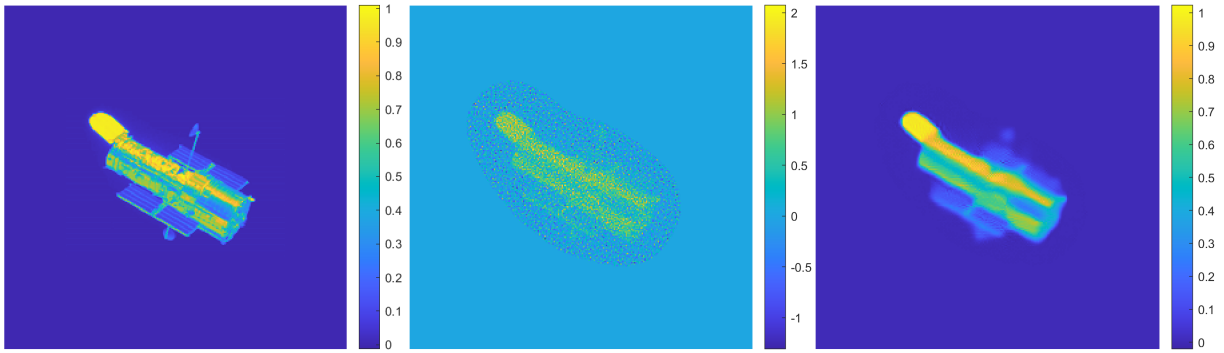

(a) (b) (c)

Figure 14: Comparison of ideal image, recovered image, and denoised image. (a) Ideal image of HST. (b) Image recovered by Dantzig Selector. SSIM = 0.772. (c) Image after removing noise from the recovered image by BM3D algorithm. SSIM = 0.932.

5.2.2 Noise-Affected PSF Map

In the previous simulation, it is assumed that the PSF map is affected by imaging constraints, such as object size and pixel resolution of the PSF sensor, but that the generated PSF map is error free. This is, of course, not realistic.

Noise in the reconstructed PSF map is linearly mapped to noise in the sensing matrix, which is used in the image recovery process. The dynamic range of the sensing matrix generated in the previous section is between 0.0249 ($\equiv p_{min}$) and 0.1016. Defining a Gaussian white noise three-sigma interval of the noise can be assumed to be smaller than p_{min}. The standard deviation of the noise is hence expressed in terms of percentage of p_{min} and five noise levels have been simulated: 2%, 10%, 15%, 20%, and 25%. Figure 15 compares a slice of sensing matrix with and without the additive white Gaussian noise. The first row of the sensing matrix is selected, and its entries are plotted. The added noise level is 25%, which is the largest noise level used in this experiment.

Given the noisy sensing matrix and light curve, the same process of image recovery as in the prevous section is used via the Dantzig Selector, and subsequent denoising using the BM3D method.

Figure 16 show the results of reconstruction and denoising for the HST with the true object displayed in Figure 7. There is clearly a degradation in the image quality of the results of all noise levels, compared to the reconstruction

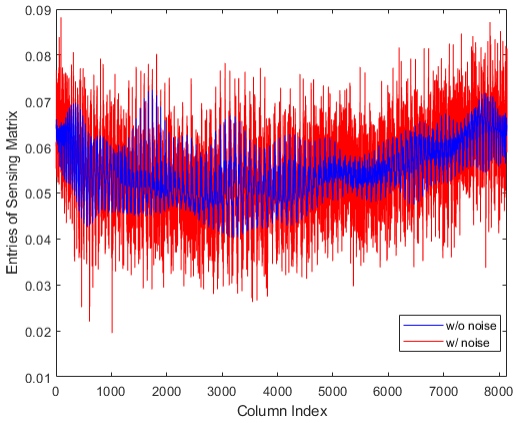

Figure 15: Comparison of a slice of sensing matrix with/without noise. The noise level is 25%.

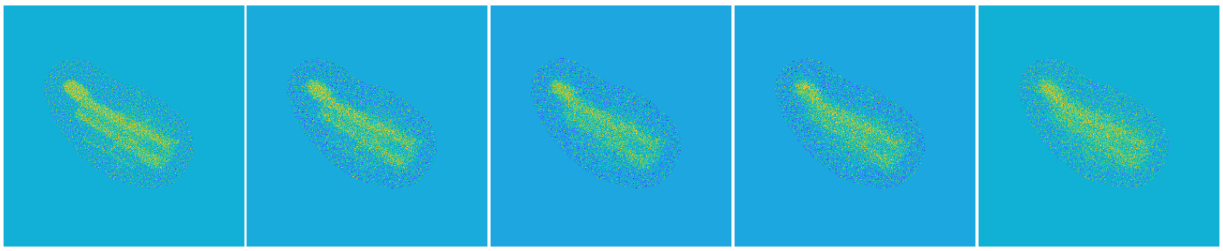

(a) σ: 2%, SSIM: 0.768 (b) 10%, SSIM: 0.764 (c) 15%, SSIM: 0.762 (d) 20%, SSIM: 0.762 (e) 25%, SSIM: 0.761

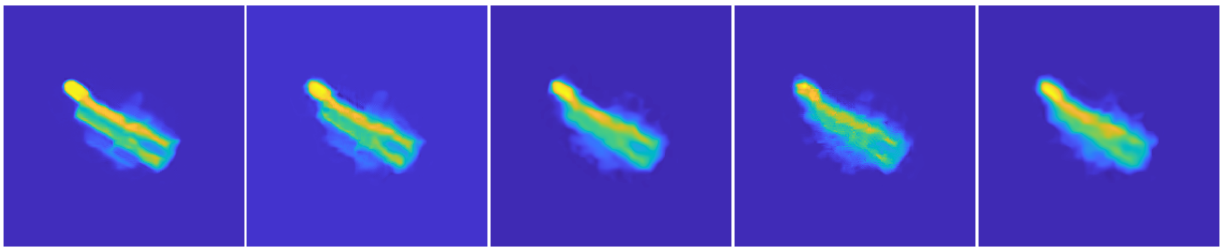

(f) 2%, SSIM: 0.927 (g) 10%, SSIM: 0.910 (h) 15%, SSIM: 0.898 (i) 20%, SSIM: 0.896 (j) 25%, SSIM: 0.890

Figure 16: Reconstruction and noise removal of images for the HST with a noise corrupted PSF, resulting in a corrupted sensing matrix. Top row: Recovered images for a noise level of (a) 2%, (b) 10%, (c) 15%, (d) 20%, and (e) 25%. Bottom row: denoised versions of the recovered images directlys above using the BM3D method.

using the perfect PSF map displayed in Figure 14.

The denoising using BM3D method is certainly necessary at the higher noise levels surpassing 10%. Especially, the solar panels of the HST become difficult to identify in the results for noise level of 20% and 25%. However, with the help of BM3D algorithm, even at the highest noise level details are still clearly discernable and a SSIM value of 0.890 is achieved. These results show the robustness of the model to the inherent noise of the PSF estimation.

6. CONCLUSIONS

This paper shows the characterization of a stabilized object in Low Earth Orbit (LEO) using optical ground-based observations. The method requires rapid imaging. The inputs are a point spread function (PSF) map in the semi-resolved scheme and an entirely unresolved light curve. The sensor obtaining the PSF and the light curve can be identical, or the light curve sensor can have a smaller aperture.

General difficulties in the traditional characterization of space object properties from light curves are circumvented by adapting the compressed sensing paradigm known from image compression because no three-dimensional model is reconstructed, but only a two-dimensional projection. In other words, a resolved image of the object of interest is recovered.

For the most realistic simulation, light propagation through free space and atmospheric turbulence is simulated in high fidelity. For the propagation through atmospheric turbulence, anisoplanatic imaging using Monte Carlos phase screens has been applied. Illustrations of the resulting degraded imaging for various object sizes have been shown.

Using the simulations, the incoherent PSF is used to generate a PSF map, which serves as the sensing matrix. Using the Dantzig selector allows avoiding the Restricted Isometry Property requirement for the sensing matrix, which is not fulfilled for a realistic PSF map. Assuming that the PSF map is perfectly known, near-perfect image recovery is possible. Even with noise levels up to 25% in standard deviation, resolved image reconstruction with insights into object surface details is possible when the resultant image is denoised after initial reconstruction.

7. ACKNOWLEDGMENTS

This work has been supported by FA9550-18-1-0154. Thank you!

REFERENCES

[1] ESA's Space Debris Office. Space debris by the numbers. `https://www.esa.int/Safety_Security/Space_Debris/Space_debris_by_the_numbers`, 2021. Online; accessed 2 April 2021.

[2] B. Kaasalainen and J. Torpa. Optimization Methods for Asteroid Lightcurve Inversion I. Shape Determination. *Icarus*, 153:24 – 36, 2001.

[3] B. Kaasalainen, J. Torpa, and K. Muinonen. Optimization Methods for Asteroid Lightcurve Inversion II. The Complete Inverse Problem. *Icarus*, 153:37 – 51, 2001.

[4] P. Magnusson et al. Determination of Pole Orientations and Shapes of Asteroids. *Asteroids II (edited by R. Binzel et. al.)*, 153:24 – 36, 1981.

[5] D. Hall, C. Brandoch, K. Knox, M. Bolden, and P. Kervin. Separating Attitude and Shape Effects for Non-resolved Objects. In *Proceedings of the 2007 AMOS Technical Conference, 16-19 September 2007, Maui, Hawaii, USA*, 2007.

[6] B. Calef, J. Afrikano, B. Birge, and P. Kervin. Photometric Signature Inversion. *Unconventional Imaging II ed. Gamiz, V., Proceedings of SPIE*, 6307, 2006.

[7] P.W. Kervin, D. Hall, M. Bolden, and J. Toth. Phase Angle: What is it good for? In *Proceedings of the 2010 AMOS Technical Conference, 14-17 September 2010, Maui, Hawaii, USA*, 2010.

[8] R. Linares, M. K. Jah, F. A. Leve, J. L. Crassidis, and T. Kelecy. Astrometric and photometric data fusion for inactive space object feature estimation. In *Proceedings of the International Astronautical Federation*, Cape Town, South Africa, Sept. 2011. Paper ID: 11340.

[9] D. Gaylor and J. Anderson. Use of Hierarchical Mixtures of Experts to Detect Resident Space Object Attitude. In *Advanced Maui Optical and Space Surveillance Technologies Conference*, page 70, September 2014.

[10] Richard Linares, Moriba K Jah, and John L Crassidis. Space object area-to-mass ratio estimation using multiple model approaches. *Advances in the Astronautical Sciences*, 144:55–72, 2012.

[11] Moriba Jah and R. Madler. Rso feature identification using hierarchical mixtures of experts. In *Proceedings of the Advanced Maui Optical and Space Surveillance Technologies Conference*, Wailea, Maui, HI, 2013.

[12] M. Holzinger, K. T. Alfriend, C. J. Wetterer, K. K. Luu, C. Sabol, and K. Hamada. Photometric attitude estimation for agile space objects with shape uncertainty. *Journal of Guidance, Control, and Dynamics*, 37(3):921–932, 2014.

[13] A. Buzzioni, S. Fan, C. Frueh, G. Altavilla, I. Foppiani, M. Micheli, J. Nomen, and N. Sanchez-Ortiz. The puzzling case of the deep-space debris WT1190F: a test bed for advanced SSA techniques. In *Stardust Conference on Asteroids and Space Debris, ESTEC, Netherlands*, 2016.

[14] D. Kucharski and et al. Full attitude state reconstruction of tumbling space debris TOPEX/Poseidon via light-curve inversion with Quanta Photogrammetry. *AActa Astronautica*, 187:115.

[15] R. Scott, A. Ellery, and M. Levesque. Non-resolved detection of objects performing On Orbit Servicing in Geostationary orbit. In *Proceedings of the 2011 AMOS Technical Conference, 14-17 September 2010, Maui, Hawaii, USA*, 2011.

[16] T. Yanagisawa and Kurosaki H. Shape and motion estimate of LEO debris using light curves. *Advances in Space Research*, 50, 2012.

[17] R. Linares, M.K. Jah, J.L. Crassidis, and C.K. Nebelecky. Space object shape characterization and tracking using light curve and angles data. *AIAA Journal of Guidance, Control, and Dynamics*, 1(1):13–25, 2014.

[18] Siwei Fan and Carolin Frueh. A direct light curve inversion scheme in the presence of measurement noise. *Journal of Astronautical Sciences*, 67:740–761, 2020.

[19] A. Buzzioni, S. Fan, C. Frueh, G. Altavilla, I. Foppiani, M. Micheli, J. Nomen, and N. Sanchez-Ortiz. Physical characterization of the deep-space debris WT1190F: a testbed for advanced SSA techniques. *Advances in Space Research*, 1(63):371–393, 2019.

[20] Richard Linares and John L. Crassidis. Space-object shape inversion via adaptive hamiltonian markov chain monte carlo. *Journal of Guidance, Control, and Dynamics*, 41(1):47–58, 2018.

[21] R. Furfaro, R. Linares, and V. Reddy. Shape identification of space objects via light curve inversion using deep

learning models. In *Advanced Maui Optical and Space Surveillance Technologies Conference*, 2019.
[22] P. Talon D. Petit E. Kerr, G.P. Elisabeth. Using ai to analyse light curves for geo object characterisation. In *Advanced Maui Optical and Space Surveillance Technologies Conference*, 2021.
[23] Stephen R. Gagnon and John L. Crassidis. *Augmenting Light Curve Based Attitude Estimation with Geometric Information*.
[24] J. Silha, T. Schildknecht, J.N. Pittet, D. Bodenmann, R. Kanzler, P. Kaerraeng, and H. Krag. Comparison of ENVISAT's attitude simulation and real optical and SLR observations in order to refine the satellite attitude model. In *Proceedings of AMOS Conference, Maui, Hawaii*, 2016.
[25] J. Silha, T. Schildknecht, J.-N. Pittet, G. Kirchner, M. Steindorfer, D. Kucharski, D. Cerutti-Maori, J. Rosebrock, S. Sommer, L. Leushacke, P. Kaerraeng, R. Kanzler, and H. Krag. Debris Attitude Motion Measurements and Modelling by Combining Different Observation Techniques. *JBIS*, 70:52.
[26] J. Silha, J.-N. Pittet, T. Schildknecht, and M. Hamara. Apparent rotation properties of space debris extracted from photometric measurements. *Advances in Space Research*, 61, 2018.
[27] T. Schildknecht and J. Silha. Determining and Modeling Space Debris Attitude States by Fusing Data from different Observation Techniques. In *Proceedings of the 7th European Conference on Space Debris, Darmstadt, Germany*, 2017a.
[28] T Schildknecht, J. Silha, J.-N.l Pittet, and Abdul Rachman. Attitude states of space debris determined from optical light curve observations. In *Proceedings of the 1st IAA Conference on Space Situational Awareness (ICSSA), Orlando, FL, USA*, 2017b.
[29] A. Rachman, A. Vananti, and T. Schildknecht. Understanding the oscillating pattern in the rotational period evolution of several GLONASS satellites. In *Proceedings of AMOS Conference, Maui, Hawaii, (Virtual Conference)*, 2020.
[30] F. Santoni, Cordelli E., and Piergentili F. Determination of disposed-upper-stage attitude motion by ground-based optical observations. *Journal of Spacecraft and Rockets*, 50, 2013.
[31] H.Y. Lin and Zhao C.Y. An estimation of Envisat's rotational state accounting for the precession of its rotational axis caused by gravity-gradient torque. *Advances in Space Research*, 61, 2018.
[32] Daigo Kobayashi and Carolin Frueh. Compressed sensing for satellite characterization. AIAA/AAS Astrodynamics Specialist Conference, 2020.
[33] Emmanuel J Candes, Justin K Romberg, and Terence Tao. Stable signal recovery from incomplete and inaccurate measurements. *Communications on Pure and Applied Mathematics: A Journal Issued by the Courant Institute of Mathematical Sciences*, 59(8):1207–1223, 2006.
[34] David L Donoho. Compressed sensing. *IEEE Transactions on information theory*, 52(4):1289–1306, 2006.
[35] Michael C Roggemann and Byron M Welsh. *Imaging through turbulence*. CRC press, 1996.
[36] David L Fried. Statistics of a geometric representation of wavefront distortion. *JoSA*, 55(11):1427–1435, 1965.
[37] Jason Daniel Schmidt. Numerical simulation of optical wave propagation: With examples in matlab. SPIE, 2010.
[38] Russell C Hardie, Jonathan D Power, Daniel A LeMaster, Douglas R Droege, Szymon Gladysz, and Santasri Bose-Pillai. Simulation of anisoplanatic imaging through optical turbulence using numerical wave propagation with new validation analysis. *Optical Engineering*, 56(7):071502, 2017.
[39] RG Lane, A Glindemann, and JC Dainty. Simulation of a kolmogorov phase screen. *Waves in random media*, 2(3):209, 1992.
[40] David George Voelz. *Computational fourier optics: a MATLAB tutorial*. SPIE press Bellingham, WA, 2011.
[41] Emmanuel J Candès et al. Compressive sampling. In *Proceedings of the international congress of mathematicians*, volume 3, pages 1433–1452. Madrid, Spain, 2006.
[42] Emmanuel Candes and Terence Tao. The dantzig selector: Statistical estimation when p is much larger than n. *The annals of Statistics*, 35(6):2313–2351, 2007.
[43] Stephen Boyd and Lieven Vandenberghe. *Convex optimization*. Cambridge university press, 2004.
[44] Zhou Wang, Alan C Bovik, Hamid R Sheikh, and Eero P Simoncelli. Image quality assessment: from error visibility to structural similarity. *IEEE transactions on image processing*, 13(4):600–612, 2004.
[45] NASA. About the Hubble Space Telescope. `https://www.nasa.gov/mission_pages/hubble/story/index.html`.
[46] Ymir Mäkinen, Lucio Azzari, and Alessandro Foi. Collaborative filtering of correlated noise: Exact transform-domain variance for improved shrinkage and patch matching. *IEEE Transactions on Image Processing*, 29:8339–8354, 2020.